Chapter 17

Energy Production, Decontamination, and Hydrogenation Reactions over Perovskite-Type Oxide Catalyst

Gina Pecchi, Nestor Escalona, I. Tyrone Ghampson and Ruddy Morales

Additional information is available at the end of the chapter

http://dx.doi.org/10.5772/61522

Abstract

Heterogeneous catalysis is an important tool in industrial processes because of the recoverability of the catalysts. Transition metal perovskites-type oxides, with the general formula ABO_3, offer attractive alternative to noble metal catalysts due to their high activity, high thermal stability, and low cost. Moreover, their physicochemical properties can be tailored to create a family of catalysts by varying the compositions of A and B. Indeed, the partial substitution at the A- and/or B-site with another metal cation stabilizes unusual oxidation states of the B cation with the simultaneous formation of structural defects. In particular, lanthanum-based perovskites have been used extensively and can be grouped into: (i) perovskites with oxygen vacancies as catalysts for oxidation reactions and (ii) perovskites as precursors to prepare nanosized catalysts for hydrogenation reactions. This chapter focuses on the use of pure and doped lanthanum perovskites as active and selective heterogeneous catalysts for catalytic energy production reaction (DME combustion), decontamination reactions (methane, acetyl acetate, toluene, n-hexane, and soot combustion), and hydrogenation reactions (guaiacol, glycerol, and xylose hydrogenation).

Keywords: Lanthanum, substituted, oxidation, hydrogenation, energy

1. Introduction

Perovskite-type oxides have been extensively studied since the pioneering work of Voorhoeve et al. [1] in the early 1970s on their potential as a cheaper alternative to noble metals as an automobile exhaust catalyst. Since then, the literature has been inundated with studies expanding their applications, particularly involving their use in combustion. Perovskites have

been demonstrated to be effective in several oxidation reactions. For environmental processes, the main objective is to achieve high conversions with almost no by-products or pollutants. Recently, there has been a particular emphasis on developing catalysts capable of either transforming pollutants into less harmful products or valorizing the by-products.

The tendency of perovskites to form unique structures is responsible for their reactivity. In general, perovskite-type oxides are represented by the general formula ABO_3, wherein the larger A-site metals, usually rare earth metals, have a dodecahedral coordination and the smaller B-site elements, first-row transition metals, have a sixfold coordination. The ability to tailor the properties of perovskites due to the different combinations of elements employed and the high degree of flexibility in their composition allow for their use in a wide range of applications.

In heterogeneous catalysis, the creation of oxygen vacancies, generally obtained by substitution in the A- and B-site, accounts for their use in catalyzing chemically and environmentally relevant reactions, such as oxidation reactions. For pure perovskites-type oxides (ABO_3), the combustion activity is dependent mainly on the B component oxides. In our previous work, we have mainly utilized Mn, Fe, Co, and Ni for the B-site of the perovskite-oxides due to their high catalytic activities; on the other hand, we have exclusively used La cation for the A-site position.

In addition to the research conducted into perovskite-based oxidation reactions, advances in preparation methods have led to perovskites being used as precursors to prepare nanosized catalysts for hydrogenation reactions. This is achieved by reduction or reduction–oxidation cycles of perovskites-type oxides under controlled conditions to leave the metal in the B-site in a high degree of dispersion on a matrix of the Ln_2O_3 oxide. Studies have demonstrated that during the reduction–oxidation cycles of $LnCoO_3$ (Ln = La, Pr, Nd, Sm, Gd) perovskites, the stability of the perovskite is affected by the nature of the Ln, with the largest lanthanide ion in the series, La, forming the most stable perovskite structure.

This chapter focuses on the use of lanthanum perovskites as active and selective catalysts in heterogeneous reactions for catalytic energy production, decontamination, and hydrogenation reactions.

2. Energy production

2.1. Fischer-Tropsch reaction

The Fischer-Tropsch synthesis (FTS) is the most important catalytic process for the synthesis of gasoline and/or diesel from syngas (a mixture of CO and H_2 formed by methane reforming) [2]. Efforts are being made worldwide to shift from conventional feedstock such as coal due to their negative environmental impact, and biomass appears to be an attractive alternative as a feedstock for the production of hydrocarbons. The gasification of biomass stream produces a gas mixture called "biosyngas" consisting mainly of CO_2, CO, CH_4, H_2, and N_2. The H_2/CO ratio in the resulting biosyngas is close to 1 and can be adjusted using the water–gas shift

http://dx.doi.org/10.5772/61522

reaction. The advantages of hydrocarbons produced from FTS using a biosyngas feed include being near CO_2-neutral and being free of sulfur and nitrogen compounds. However, there is a dearth of systematic studies of catalytic systems in FTS using biosyngas [3-5]. Perovskites have been shown to be highly active in FTS using a H_2/CO mixture, and its activity was related to the properties of the perovskite precursor: stability, crystalline structure, and degree of reduction [6, 7]. These results paved the way for the evaluation of perovskites for FTS of biosyngas. Hence, this study was focused on FTS over $LaFe_{1-x}Co_xO_3$ perovskites using biosyngas as the feed.

2.2. B-site substitution

The FTS reaction using a simulated gas mixture similar to biosyngas over $LaFe_{1-x}Co_xO_3$ perovskites presented a wide distribution of liquid hydrocarbons (C_6 to C_{18+}) and a high production of CH_4 attributed to Co metal segregation on the surface. The distribution of the liquid products was related to the average size of iron particles [8].

A series of $LaFe_{1-x}Co_xO_3$ perovskites ($0.0 \leq x \leq 1.0$) were prepared using the amorphous citrate precursor method and characterized by N_2 physisorption, X-ray diffraction (XRD), Fourier-transform IR spectroscopy (FTIR), O_2-Temperature programmed desorption (O_2-TPD), Thermal-programmed reduction (TPR), and Scanning electron microscopy (SEM). FTS was carried out in a stainless steel fixed-bed reactor at 300°C and 1 MPa. The BET surface areas of the samples (13 m^2g^{-1}) were as expected for these kinds of structures. The reduction behaviors of the catalysts (TPR_1-TPR_2) are shown in Fig. 1. This analysis provides information on the thermal stability of the catalyst (segregation of Co particles) under reducing conditions, deduced from the reducibility of the oxide precursor. The procedure involved: (i) a first reduction step under H_2/Ar flow up to 700°C (TPR_1); (ii) cooling under Ar flow to room temperature; (iii) an oxidation step under flowing O_2/He mixture up to 700°C; and (iv) a second reduction treatment (TPR_2) as in step 1. Figure 1 shows that the largest differences between TPR_1 and TPR_2 were observed for pure $LaFeO_3$ and $LaCoO_3$ perovskites, while the substituted perovskites showed similar profiles. Pure $LaFeO_3$ is essentially irreducible. On the other hand, the profile for pure $LaCoO_3$ revealed two well-defined peaks: a peak at 350°C is indicative of the formation of an oxygen-deficient perovskite structure, while the second peak above 500°C corresponds to the complete reduction of the perovskite to form Co^0. The substitution of Fe^{3+} by Co^{3+} affected the initial reduction stage, showing only one reduction peak, probably by passing an intermediate reduction state. The subsequent reduction of Co^{3+}/Co^{2+} to Co^0 occurred at a higher temperature, then decreased in intensity with increasing Fe, and subsequently disappeared when the level of substitution reached 50%. The slight difference in the TPR_2 profiles in comparison with TPR_1 is indicative of the reversibility of the redox cycle. The small and broad peaks observed at 410°C for $LaFeO_3$ in the TPR_2 profile are associated with Fe^{3+} segregation during the first reduction step, since this perovskite is a Co-free sample and La is not reducible under the experimental conditions. Thus, during TPR_1, metallic iron is expelled from the perovskite structure at 620°C. The quantification of the first reduction peak at temperatures below 500°C is representative of the extent of Co insertion into the perovskite structure: our data revealed a near linear increase in hydrogen consumption with x, an

indication of the progressive insertion of Co into the perovskite structure. The XRD patterns of the calcined perovskites displayed two crystal systems, orthorhombic for x<0.5 and rhombohedral for x≥ 0.5. On the other hand, XRD analyses of reduced perovskite showed no significant changes after H_2 reduction, indicative of the high thermal stability of these $LaFe_{1-x}Co_xO_3$ perovskite solid solutions. The diffraction lines broadened upon substitution of Fe^{3+} by Co^{3+}, which suggests a decrease in the crystallinity. The highest stability under hydrogen was obtained for the perovskite with x = 0.5, while the thermal stability of x = 0.1 and 0.3 perovskites were similar to that of the pure $LaCoO_3$ and x = 0.4 perovskites, respectively. The observed behavior of the x = 0.2 perovskite indicates a loss in the perovskite structure, suggesting segregation of the B cation. FTIR spectra indicated that for the x ≤ 0.5 perovskites, Co^{3+} ions were incorporated into the orthorhombic $LaFeO_3$ perovskite structure and that a new rhombohedral structure appeared for x = 0.5. The pure $LaFeO_3$ tolerated Co insertion with no structural changes up to values of x ≤ 0.3. For x = 0.4 and x = 0.5, the presence of a mixture of orthorhombic and rhombohedral structures were detected. The catalytic activity indicated a high intrinsic CO conversion for the substitution degree of x = 0.1, 0.2, and 1.0, in line with their orthorhombic structures and the presence of segregated Co metal. The x = 0.2 perovskite displayed the highest CO intrinsic conversion attributed to the presence of highly dispersed, segregated Co species. The absence of segregated Co species in the x = 0.3 and 0.4 perovskites explains their lower activities. In fact, these perovskites possessed higher thermal stability under reducing atmospheres due to the presence of a mixture of orthorhombic and rhombohedral crystalline structures, which implies that they did not segregate Co species. In relation to selectivity, an increase in x led to a decrease in CH_4 selectivity, while a decrease in x favored selectivity to longer-chain length condensable hydrocarbons: this was attributed to changes in the average particle size of segregated Co species. The smaller particles of the x = 0.2 and 0.1 perovskites favored the formation of longer-chain hydrocarbons. Pure $LaCoO_3$ perovskite displayed the highest extent of poorly dispersed segregated Co, favoring the formation of short-chain hydrocarbons (C_8-C_9). Thus, the catalytic activity of $LaFe_{1-x}Co_xO_3$ perovskites in FTS can be explained in terms of the crystalline structure, segregated Co content, and particle size.

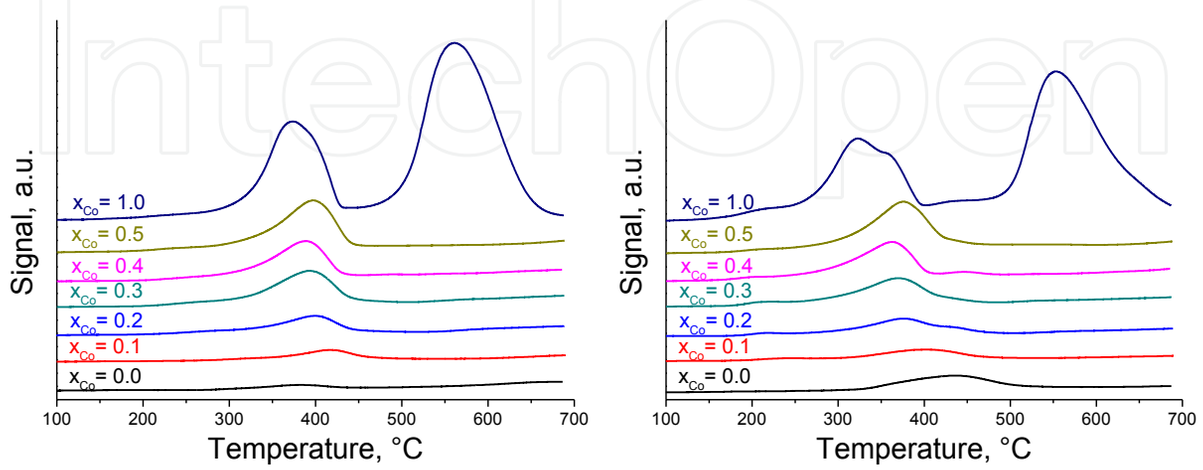

Figure 1. Temperature-programmed reduction profiles of $LaFe_{1-x}Co_xO_3$ perovskites: left: TPR_1 and right: TPR_2

http://dx.doi.org/10.5772/61522

3. Dimethyl Ether (DME) combustion

The easier transportation, lower emission of polluting particles, and higher thermal efficiency of dimethyl ether (DME) make it a useful, low-cost replacement for liquefied petroleum gas (LPG) and diesel fuel. Recently, the catalytic combustion of DME has been studied on Ce-doped manganese oxide octahedral molecular sieves (OMS-2) [9]. Mixed oxides with perovskite-type structures, in particular $LaMnO_{3.15}$, have the potential to be highly active catalysts for the deep oxidation of DME. This catalyst has been previously used for the catalytic oxidation of toluene [10], carbon monoxide [11], and NH_3 [12].

3.1. B-site substitution

The electronic properties and performance of $La(Mn_{0.5}B_{0.5})O_{3.15}$ (B = Cr, Fe, Co, Ni, Cu) perovskites in the combustion of dimethyl ether (DME) revealed that an increase in the catalytic performance, expressed as intrinsic activity ($\mu molm^{-2}h^{-1}$), is contingent on B-site substitution in $LaMnO_3$ and a decrease in the required calcination temperature to obtain the perovskite structure. The similar tolerance factor (t) of the substituted perovskites, a measure of the geometric effect, plays a secondary role on the surface and catalytic performance. Consequently, the electronic effect explains the relationship between catalytic performance, chemisorbed oxygen species, and reducibility of the substituted perovskites. XRD results indicated that calcined pure $LaMnO_{3.15}$ and Cr-, Co-, and Fe-substituted perovskites presented well-defined rhombohedral structure, whereas Cu- and Ni-doped perovskites displayed La_2CuO_4 and La_2NiO_4 phases. The largest surface area corresponded to the $LaMnO_{3.15}$ perovskite with 11 m^2g^{-1}, and subsequently decreased upon B-substitution. The TPR profiles obtained for the pure and oxygen-rich $LaMnO_{3.15}$ perovskite presented a concentration of 32% Mn^{4+} ions after H_2 reduction. An observed reduction peak at 350°C with a shoulder at 420°C corresponds to the reduction of Mn^{4+} to Mn^{3+}, followed by the destruction of the perovskite structure (Mn^{3+} to Mn^{2+}) at 800°C [13-15]. Upon B- substitution, the two reductions steps of pure $LaMnO_{3.15}$ perovskite were maintained when Co and Ni were used, while only one reduction step was detected for the Cr- and Fe-substituted perovskite. This result is closely related to the thermal behavior of nonreducible perovskites such as $LaCrO_3$ and $LaFeO_3$. Thus, Fe- and Cr-substituted perovskites showed lower reducibility compared to the parent $LaMnO_{3.15}$ but higher reducibility in comparison with the nonreducible $LaCrO_3$ and $LaFeO_3$ perovskites. The observed increase in the reducibility of the Co- and Ni-substituted perovskites is similar to the effect induced by La substitution of divalent alkaline-earth cations. The high stabilities of Co^{2+} and Ni^{2+} helped stabilize the Mn^{4+} ions, with corresponding increase in the reduction peaks. On the other hand, the TPR results for the Cu-substituted perovskite showed a single-step complete reduction of the Cu ions to the metallic state, similar to the reduction of CuO but at lower temperatures. The O_2-TPD experiments were used to evaluate the redox properties of the catalysts. The data revealed two different behaviors, consistent with the different patterns observed from TPR results: for the Cr- and Fe-substituted perovskites, a behavior similar to the parent $LaMnO_{3.15}$ perovskite was observed, with the presence of α- and β-oxygen species beginning at ~600°C. Conversely, the absence of β-oxygen at temperatures below 700°C for the Co-, Ni-, and Cu-substituted perovskites is related to the lattice oxygen-

deficient structures. XPS analyses showed that the $La3d_{5/2}$ spectra presented peaks with BE at 834.3 eV and 838.1 eV that correspond to La^{3+} in the perovskite. The small difference between the BEs of Mn^{3+} at 641.3 eV and Mn^{4+} at 642.4 eV makes it difficult to distinguish them. Regarding the Cr $2p_{3/2}$ spectra, two peaks with BEs centered at 576.6 and 579.4 eV were detected: the peaks were assigned to surface Cr^{3+} and Cr^{6+} species, respectively. The main peak of the Fe $2p_{3/2}$ spectra was located at 710.8 eV, and is attributed to surface Fe^{3+} species. For the Co $2p_{3/2}$ spectra, the two peaks detected at 780.6 and 786.9 eV are associated with Co^{3+} and Co^{2+} species, respectively. Because the Ni $2p_{3/2}$ signal coincides with the La $3d_{3/2}$ signal, the BE of Ni $2p_{1/2}$ was measured instead. The displacement of the Ni BE to 873.2 eV suggests the presence of surface Ni^{2+} species. Considering the low BET surface area of the substituted perovskites, the surface composition was similar to the nominal composition in the bulk, and the surface analysis may be extrapolated to the bulk. The BE of O 1s peak less than 532 eV suggests the absence of surface oxygen vacancies. Therefore, the substitution of Mn^{3+} with a first-row transition metal in the (III) oxidation state preserved the oxygen-rich perovskite structure for the $LaMn_{0.5}Cr_{0.5}O_{3.15}$ and $LaMn_{0.5}Fe_{0.5}O_{3.15}$ perovskites. On the other hand, the substitution by Co^{2+}, Ni^{2+}, and Cu^{2+} generated a stoichiometric cubic perovskite structure. These differences in behavior are in agreement with interpretations deduced from TPR and O_2-TPD results. The catalytic activity of the B-site substituted perovskites were tested in the combustion of DME with excess oxygen in a flow reactor. The light-off curves allow the calculation of the reaction rate of the oxidation reaction at low conversion levels (<10%) at 180°C. The reaction rate was correlated with the H_2 consumption calculated from TPR profiles and the α-oxygen derived from O_2-TPD (both parameters normalized by the specific surface area), and shown in Fig. 2. It can be inferred from this correlation that the high stability of (III) oxidation state of Cr^{3+} and Fe^{3+}cations did not increase the redox character of the Mn^{4+}/Mn^{3+} pair; on the other hand, the higher redox properties and catalytic performances of the $LaMn_{0.5}Co_{0.5}O_3$ and $LaMn_{0.5}Ni_{0.5}O_3$ catalysts stem from the high stability of (II) oxidation state of Co^{2+} and Ni^{2+}, leading to a progressive decrease of Mn^{3+} species, while stabilizing the Mn^{4+} species in the network.

4. Decontamination reactions

4.1. VOCs abatement

Metal oxides with a perovskite structure have been consistently proposed during the last two decades as alternative catalysts for the deep oxidation of hydrocarbons. It is well-known that perovskite-like mixed oxide substitution of the trivalent A-site metal ion with a bivalent or tetravalent metal cation (A') is accompanied by a modification of the oxidation state of the B-site metal cation, thus modifying its catalytic activity. Moreover, modification of the oxidation state of the B-site metal cation by insertion of A' may be accompanied by the formation of structural defects, thus leading to nonstoichiometry. This usually means the creation of oxygen defects in the Co-containing perovskites, while in the Mn-perovskites it results in excess of oxygen [13]. Fe-based [12] and Ni-based perovskites [14] were shown to exhibit an intermediate behavior. Good catalytic performances in combustion reactions were displayed by La- or

http://dx.doi.org/10.5772/61522

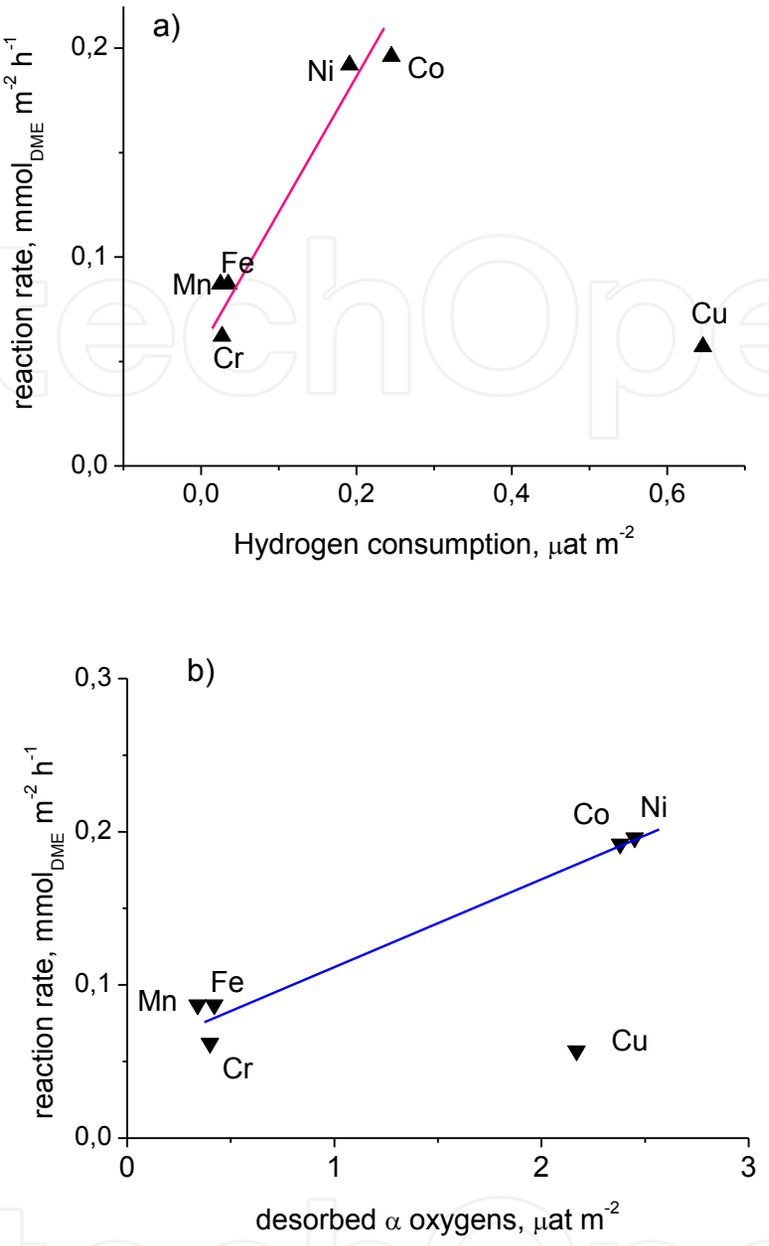

Figure 2. Intrinsic activity as a function of quantity of hydrogen consumed (above) and quantity of α-oxygen desorbed

La_xSr_{1-x}-based perovskites containing Co, Fe, or Mn as B cation [15, 16]. A major drawback for their application, however, is their low surface area, and hence significant efforts are underway to increase the specific surface area of conventional $A_{1-x}A'_xBO_{3-\delta}$ perovskites through various preparation methods [17, 18].

The insertion of calcium ions into the $LaFeO_3$ perovskite lattice results in a solid with structural and electronic defects possessing highly active sites for redox reactions. A continuous increase in number of oxygen vacancies in $LaFeO_3$ perovskites upon A-site substitution of La^{3+} by Ca^{2+} was previously reported [19]. In this work, $La_xCa_{1-x}FeO_3$ (x = 0.0, 0.1, 0.2, 0.3, 0.4) perovskites prepared by precursor citrate method were characterized and evaluated in catalytic

combustion reaction. The effect of La substitution by calcium on the physical, chemical, and catalytic properties for the total combustion of acetyl acetate and methane was studied. Surface area values ranging from 19 to 39 m^2g^{-1} were obtained as the calcium content of the perovskites varied from 0.0 to 0.4. XRD patterns indicated that for pure $LaFeO_3$ an orthorhombic perovskite structure was observed; on the other hand, a shift toward larger 2θ angles appeared as La^{3+} was partially substituted by Ca^{2+}, evidence of lattice distortion. Even though the ionic radii are very similar (La^{3+} = 0.136 nm; Ca^{2+} = 0.134 nm), the substitution of La^{3+} with a cation of lower valence like Ca^{2+} entails either the oxidation of the cation at the B-site (i.e., $Fe^{3+} \rightarrow Fe^{4+}$) or the formation of oxygen vacancies in order to retain electroneutrality. Since the ionic radius of Fe^{4+} (0.0585 nm) is smaller than that of Fe^{3+} (0.0645 nm), the distortion can be explained by the presence of Fe^{4+} in the perovskite structure, in agreement with previous results reported for other iron-based perovskites. The shift of the 2θ angles as a function of the degree of calcium substitution is illustrated in Fig. 3: a linear shift of the 2θ values is observed with increasing Ca content, a clear indication of the insertion of calcium in the studied range.

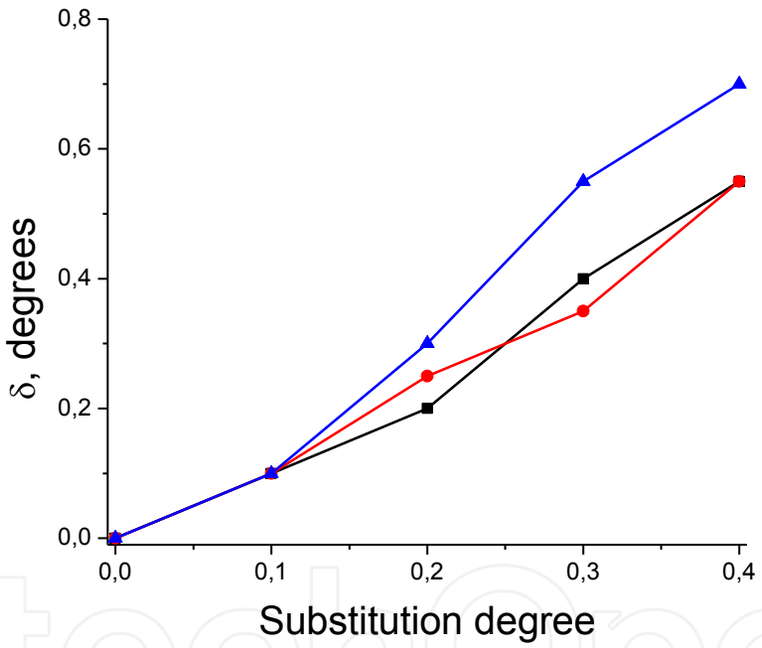

Figure 3. Shift of the peak position as a function of substitution degree 2θ (●) 40°; (■) 46°; (▲) 58°

IR spectra of the perovskites show a band at 865 cm^{-1}, attributed to O-C-O bending in the carbonates. This peak appeared as a shoulder for x = 0.1 and increased linearly when x ≥ 0.2, without showing any change in the wavelength. This band is ascribed to the presence of calcium and corresponds to the out-of-plane bending of the carbonate ions supporting the incorporation of calcium in the perovskite structure. O_2-TPD profiles showed clear increase of the desorbed oxygen as the degree of Ca substitution increased. In addition, an appreciable desorption peak was observed at temperatures above 500°C for the perovskite with the highest degree of substitution. This desorbed oxygen corresponds to the so-called β oxygen, which is associated with lattice oxygen or with oxygen species occupying the inner vacancies created

by substitution of Ca by La. The plot of the amount of O_2 desorbed from 150°C up to 700°C, which involves α-oxygen species, as a function of Ca substitution showed a continuous increase. Desorption of large amount of lattice oxygen in the bulk from the samples indicates a large substitution vacancy and/or defects. TPR profiles for the pure $LaFeO_3$ showed no reduction peaks, indicative of the nonreducibility of this perovskite. However, the TPR profile for the substituted perovskites showed a pronounced peak at lower temperatures that shifted to higher temperatures and increased in intensity as the degree of Ca substitution increased. The replacement of part of La^{3+} by Ca^{2+} led to a well-defined H_2 consumption peak due to the higher amount of Fe^{4+} ions generated to compensate for the unbalanced charge, consistent with the deduction from XRD results. In situ XRD measurements also revealed no detectable differences between diffraction patterns of pre- and post-TPR measurements, suggesting that the integrity of the structure was retained after hydrogen treatment, although the nature of the phases present in the sample changed. The post-TPR XRD pattern of the pure $LaFeO_3$ perovskite was essentially the same as that obtained for the fresh perovskite: the only difference was a minimal increase in the intensity of the peaks and small shifts toward lower angles, indicating increased crystallinity with a great expansion of the cell parameters. The catalytic activity in the oxidation of methane and acetyl acetate in a flow reactor using an excess amount of oxygen showed two contrasting behaviors: a near independency of the ignition temperature with Ca substitution for the methane reaction; and a decrease in ignition temperature with Ca substitution for the acetyl acetate reaction. These results clearly demonstrate the differences between a suprafacial and intrafacial reaction mechanism. The presence of substituted Ca ions enhances the catalytic activity of suprafacial reactions (e.g., acetyl acetate combustion), which typically occurs at lower temperatures. Conversely, the activity of intrafacial reactions (e.g., methane combustion), which requires a much higher temperature, is only slightly modified by Ca^{2+} insertion into the perovskite.

4.2. A-site substitution

A different behavior was detected upon the substitution of La^{2+} by Ca^{2+} in $LaNiO_3$ and $LaFeO_3$ perovskite-type oxides. In the Fe series ($La_{1-x}Ca_xFeO_3$), the perovskite structure is maintained within the studied range of substitution. In contrast, a completely different behavior was observed for the Ni series ($La_{1-x}Ca_xNiO_3$), whereby a Brownmillerite-type structure ($La_2Ni_2O_5$) with a large degree of segregated phase as highly dispersed mixed oxides was observed [20]. There was no monotonic dependence of the S_{BET} values on the extent of La substitution. The XRD patterns shown in Fig. 4 revealed the presence of orthorhombic structure for the Fe series; however, for the pure $LaNiO_3$ counterpart, the peak at $2\theta = 43.3°$ indicated the presence of segregated NiO. For the Ni series, the most prominent diffraction line at $2\theta = 32.7°$ changed from a singlet for x = 0.0 to a doublet for both x = 0.2 and 0.4, as shown in the inset of Fig. 4. As x increased, the diffraction line at $2\theta = 32.7°$ corresponding to $LaNiO_3$ structure decreased in intensity and, consequently, a new diffraction line at $2\theta = 32.4°$ corresponding to $La_2Ni_2O_5$ brownmillerite-type structure appeared. Additionally, NiO and CaO were also present as segregated phases for the x = 0.2 and 0.4 solids. Thus, it is difficult to substitute La^{3+} with Ca^{2+} in $LaNiO_3$ even to a limited extent. TPR profiles showed increase in the extent of reduction in the Fe series, explained by the higher amount of Fe^{4+} ions generated

to compensate for the unbalanced charge. For the Ni series, a large amount of H_2 consumption indicated a total reduction of Ni^{3+} ions in $LaNiO_3$ to yield the $La_2Ni_2O_5$ phase, followed by an H_2 consumption peak at 500°C, ascribed to Ni° deposited on La oxide. The evolution of oxygen during TPD measurements showed the expected presence of physisorbed species at low temperatures in the Fe series, in addition to α-oxygen, which appeared as a shoulder for the pure $LaFeO_3$. There was a noticeable increase in the intensity of the peak attributed to the so-called β-oxygen upon Ca^{2+} substitution. Since this peak is associated with the lattice oxygen or with oxygen species occupying inner vacancies, their evolution is a measurement of the replacement of La^{3+} by Ca^{2+} in the perovskite structure. For the Ni series, the desorption profiles for the pure $LaNiO_3$ and the substituted samples showed a large increase in the desorption peak detected at 350°C, indicative of either the presence of segregated metal oxide phases in a high degree of dispersion or crystalline oxides (such as $La_2Ni_2O_5$), as detected by XRD. With regard to the XPS spectra of the Fe series, the BE of the most intense peaks of doublets for $La3d_{5/2}$ at 834.8 eV and $Fe2p_{3/2}$ at 710.3 eV were almost constant. For the Ni counterpart, on the other hand, the overlap of the $La3d_{3/2}$ and $Ni2p_{3/2}$ peaks may mask the accurate measurement of the intensity of the Ni BE; thus, the $Ni2p_{1/2}$ was measured instead. The least intense $Ni2p_{1/2}$ peak at 873.4 eV was almost constant, and the detected satellite line at 881.2 eV is indicative of the presence of Ni^{2+} ions on the surface. The Ca $2p_{3/2}$ doublet has two peaks at BE of 346.2 and 346.8 eV, corresponding to surface Ca-O and carbonated surface Ca^{2+} ions, respectively. O1s peak was deconvoluted into three components: at BE of 529.2 eV assigned to surface O^{2-} species, at 531.0 eV which arises from lattice [La-O-M] bonds and at 532.3 eV due to hydroxyl/carbonate groups. In the Fe series, x = 0.2 showed the largest extent of Ca incorporated into the perovskite structure at 346.2 eV, while a clear trend was not observed for the Ni series. The (Fe/La+Ca) and (Ni/La+Ca) surface ratios were higher than the nominal compositions: i.e., the solid surface became enriched with Ni and Fe. Since the carbonation degree is related to the extent of segregated phases, the (CO_3^{2-}/La+Ca) surface ratio for the Fe and Ni series can provide an insight into the surface structure of the solid. A decrease in the carbonation degree upon Ca substitution was obtained for the Ca series; conversely, a larger increase with increasing x was detected for the Ni series. This finding is in agreement with the previous characterization results, and demonstrates that upon Ca substitution, Ni^{3+} ions are more difficult to stabilize than Fe^{3+} ions in the perovskite lattice. The perovskites were tested in toluene combustion (4000 ppmv) in a flow reactor under an excess of oxygen using a GHSV of 47000 h^{-1}. For the Fe series, the substituted perovskites displayed higher catalytic activity than the pure $LaFeO_3$ perovskite and the maximum catalytic activity was obtained for the perovskite with x = 0.2. The observed trend in activity indicated no simple dependence on the metal ion oxidation state, and appeared to be due to the effect of the pair Fe^{4+}/Fe^{3+} on the vacancy ordering, in that a disordered distribution of oxygen vacancies led to an increase in the catalytic activity. The lower activation energy displayed by $La_{0.8}Ca_{0.2}FeO_3$ can be attributed to cationic vacancies compensating the amount of Fe^{4+} involved in the reaction. Conversely, for the Ni series, substitution resulted in solids with lower activity than the pure $LaNiO_3$ perovskite due to the loss of the perovskite structure and the corresponding change in the oxidation state of Ni^{3+} to Ni^{2+}.

http://dx.doi.org/10.5772/61522

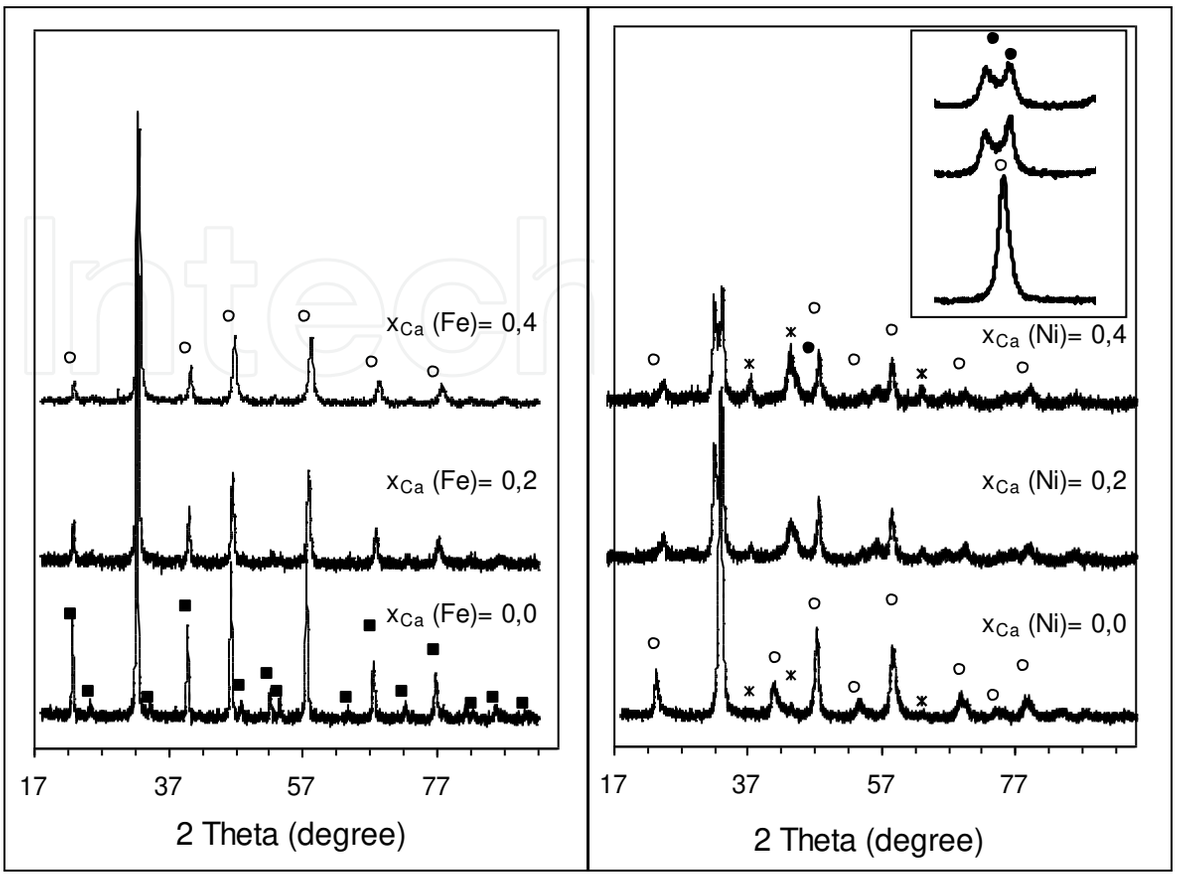

Figure 4. X-ray diffraction patterns of (a) $La_{1-x}Ca_xFeO_3$: (■) orthorhombic; (○) cubic $LaFeO_3$; (b) $La_{1-x}Ca_xNiO_3$; (○)$LaNiO_3$; (■) NiO; (●) $La_2Ni_2O_5$

4.3. B-site substitution

The catalytic activity expressed as intrinsic activity (mol m^{-2} h^{-1}) for the total combustion of acetyl acetate and ethanol over substituted $LaFe_{1-y}Ni_yO_3$ perovskites revealed that the simultaneous presence of Ni^0 and Ni^{2+} is required to achieve optimum performance for these perovskites-type oxides [21]. The largest BET surface area of 20 m^2g^{-1} was obtained for the unadulterated $LaFeO_3$ perovskite, and then decreased progressively upon Ni substitution. XRD patterns indicated an orthorhombic phase for $LaFeO_3$ and a rhombohedral phase for $LaNiO_3$. Upon substitution of Fe^{3+} ions by Ni^{3+} ions, a shift toward larger 2θ angles was observed. The shift of the peak reached a maximum for a substitution degree y = 0.1, and then remained constant for higher substitutions. These findings suggest complete insertion of nickel for substitution y = 0.1, whereas a simple mixed NiO_x phase became segregated for substitutions y> 0.1. FTIR spectra indicated that upon Ni^{3+} substitution the band at 560 cm^{-1} shifted toward higher wavenumbers and increased in intensity compared to that for pure $LaFeO_3$. The dependence of these two parameters on the substitution degree runs in parallel with the shift observed in the main diffraction lines of the XRD patterns, confirming that Ni^{3+} ions were incorporated within the perovskite structure. The TPR_1-TPR_2 cycles of the substituted perov-

skites did not show significant differences between them, indicating that their structures were restored after intermediate oxidation. No reduction peaks were observed for the nonreducible $LaFeO_3$, while two reduction peaks were observed for $LaNiO_3$, attributed to reduction of Ni^{3+} ions of $LaNiO_3$ to yield $La_2Ni_2O_5$. The second reduction peak at 500°C led to Ni^0. Only one less-intense peak was observed for the substituted perovskite with almost no change in intensity (in comparison with TPR_2), indicative of the high stability of $LaFe_{1-y}Ni_yO_3$ (y = 0.1, 0.2, 0.3). The evolution of oxygen during TPD experiments indicated the presence of α-oxygen in the pure $LaNiO_3$ and the two highest substituted perovskites. The intensity of the desorption peaks increased as the degree of substitution increased. There was no evidence of the presence of α-oxygen on substituted perovskite with y = 0.1, and this was related to the absence of segregated metal oxide phases in this sample. The BEs of the XPS spectra for O1s was deconvoluted into three components: 529.2 eV attributed to surface O^{2-} species; 531.0 eV, which arose from lattice [La-O-M] bonds; and 532.3 eV, which was due to hydroxyl/carbonate groups. The intensity of the two peaks at 529.2 eV and 531.0 eV changed almost linearly in a perfect opposite way, which was related to the incorporation of Ni into the structure. The increase in intensity of the lattice oxygen component in the sample with increase in Ni substitution was related to the increasing catalytic activity in combustion reactions. The surface atomic ratios Fe/La, Ni/La, and CO_3^{2-}/La was plotted as a function of Ni substitution degree and shown in Fig. 5: upon Ni substitution, the surface of the substituted perovskites became Ni- and Fe-enriched. The Fe/La surface ratio for the nonsubstituted $LaFeO_3$ is consistent with the slight La-enrichment often reported for La-containing perovskites, whereas the larger Ni/La surface ratio for $LaNiO_3$ and also for the substituted $LaFe_{1-y}NiO_3$ samples indicated that Ni^{3+} ions are more difficult to be stabilized than Fe^{3+} ions in the perovskite lattice and results in surface segregation of a separate NiO phase. The extent of carbonation was higher for $LaFeO_3$ due to basic character of the slight La-enrichment observed in this perovskite. The catalytic activity tested in the combustion of acetyl acetate and ethanol in a flow reactor under an excess of oxygen showed differences in catalytic behavior depending on the nature of the substrate to be combusted. Ethanol reacted at lower temperatures and exhibited a higher reaction rate. The catalytic activity of $LaFeO_3$ increased upon nickel substitution but declined for $LaNiO_3$. The approach undertaken to modulate oxygen adsorption and release properties by inserting Ni^{3+} ions into the $LaFe_{1-y}Ni_yO_3$ structure while retaining a separate NiO phase is crucial to enhance the performance of substituted perovskites in the combustion of ethanol and acetyl acetate.

4.4. B-site substitution

For substituted $LaMn_{1-y}Co_yO_3$ perovskite-type oxides, a crystal phase transformation occurred for y values above 0.5 and the general trend obtained was: for y ≤0.5, Co ions were inserted into the manganite structure; for y >0.5, the Mn ions were inserted into the cobaltite structure. The enhancement of the ferromagnetic properties and the thermal stability against reduction for y = 0.5 was attributed to the optimized Co^{2+}-Mn^{4+} interactions [22, 23].

The manganite had the highest surface area (38 m^2g^{-1}), and that upon Co substitution, a progressive decrease in surface area was observed until reaching the cobaltite surface value of 16 m^2g^{-1}. XRD analysis showed the existence of cubic and rhombohedral perovskites phases

http://dx.doi.org/10.5772/61522

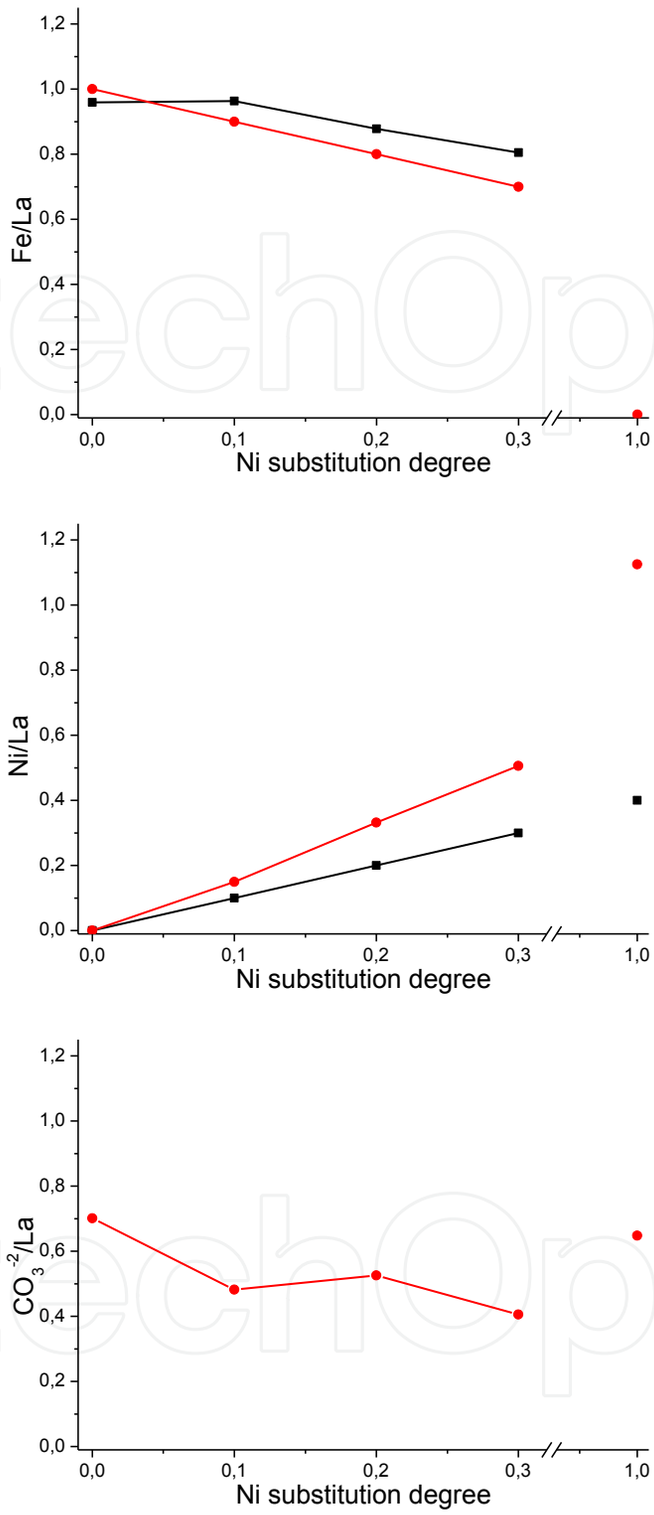

Figure 5. XPS ratios for the $LaFe_{1-y}Ni_yO_3$ perovskite: (■) atomic surface ratio, (●) nominal (a) Fe/La, (b) Ni/La, (c) CO_3^{2-}/La

for pure $LaMnO_3$ and $LaCoO_3$, respectively. The general trend obtained for the $LaMn_{1-y}Co_yO_3$ perovskites were as follows: (i) the XRD patterns were quite similar to the cobaltite's rhom-

bohedral structure for the y>0.5 samples; (ii) the structure of the perovskite was modified to form a new orthorhombic structure for y<0.5; (iii) and for the case of y=0.5, the pattern was practically equal to the one obtained for pure $LaMnO_3$. The vibration frequencies in the infrared region allowed us to conclude that the insertion of Mn into the cobaltite resulted in notable distortions of the highly symmetrical rhombohedral structure, and that manganite can withstand Co insertion without large structural changes up to values of $y \leq 0.3$. With regard to TPR profiles, $LaCoO_3$ and $LaMnO_3$ displayed two reduction peaks, ascribed to the formation of oxygen-deficient intermediate and the reduction of the perovskite structure at higher temperatures. The substituted perovskites exhibited nearly identical behavior with temperature displacements, which was attributed to the previously discussed distortions. The magnetic properties were investigated in the paramagnetic and magnetically ordered regimes: in both cases the data revealed two well-identified regions separated by the equimolar composition y = 0.5. For samples with y > 0.5 (Mn substitutes Co in the cobaltite $LaCoO_3$) the Curie-Weiss temperature sharply decreased, reaching negative values at y = 1. This nonmonotonous variation was also observed in the ordering temperature T_c, which reached a maximum value for y = 0.5. The magnetic moment of the paramagnetic regime showed a linear decrease during the first half of the cobalt substitution, which was interpreted as the progressive transformation of Mn^{3+} into Mn^{4+} ions. This decrease became more pronounced above y = 0.5 since Mn ions were all converted to Mn^{4+}, and cobalt was being introduced as Co^{3+}. The overall behavior observed through the compositional variation of the Curie-Weiss temperature is explained by the varying character of the magnetic interactions between Co and Mn. During the first half of the series ($y \leq 0.5$), strong Co^{2+}-Mn^{4+} double-exchange ferromagnetic interactions were triggered when Co^{2+} was introduced into the lattice, while antiferromagnetism was augmented when Co was introduced as Co^{3+} (y>0.50). To investigate the ordered regime, the thermal dependence (ZFC/FC cycles) and the field dependence (M loops) of the magnetization was carried out. Figure 6 compares the (ZFC/FC cycles) regions separated by the equimolar composition y = 0.5. A strong ferromagnetic behavior was observed for the first half of the series since the magnetization M_{FC} reached a characteristic plateau and the ordering temperature increased toward a maximum value of 235 K. For y compositions above 0.5, the magnetization decreased by one or two orders of magnitude, meaning that the ferromagnetic Co^{2+}-Mn^{4+} interactions were weaker, being progressively replaced by the less effective Co^{2+}-Co^{3+} interactions. Thus, magnetic iso-field studies (ZFC-FC) revealed that, for $y \leq 0.50$, the system presented an antiferromagnetic canted-like ordering of the Mn/Co sublattice, in which the presence of divalent Co ion created Mn^{3+}-Mn^{4+} pairs that interact ferromagnetically through the oxygen orbital. This was confirmed by the magnetization loops in which the magnetic moment increased when substituting Mn for Co. The catalytic activity in total acetyl acetate combustion in a flow reactor under an excess of oxygen (60000 $cm^3g^{-1}h^{-1}$) indicated that lower ignition temperature (i.e., the higher activity) was displayed by manganite, while higher ignition temperature was exhibited by the cobaltite. The substituted perovskite displayed ignition temperatures between these two values, indicating that changes in y values modified the active sites required for the oxidation of organic compound. The larger intrinsic activity ($molm^{-2}h$-1) of the substituted perovskites with y= 0.5 was attributed to the magnetic order of Mn^{4+}-Co^{2+}. This ordered state confirmed the presence of two regimes, separated by the

http://dx.doi.org/10.5772/61522

equimolar composition $LaMn_{0.5}Co_{0.5}O_3$: strong ferromagnetic interactions for $y_{Co} \leq 0.5$ and a superposition of antiferromagnetism and ferromagnetism for $y_{Co} > 0.5$.

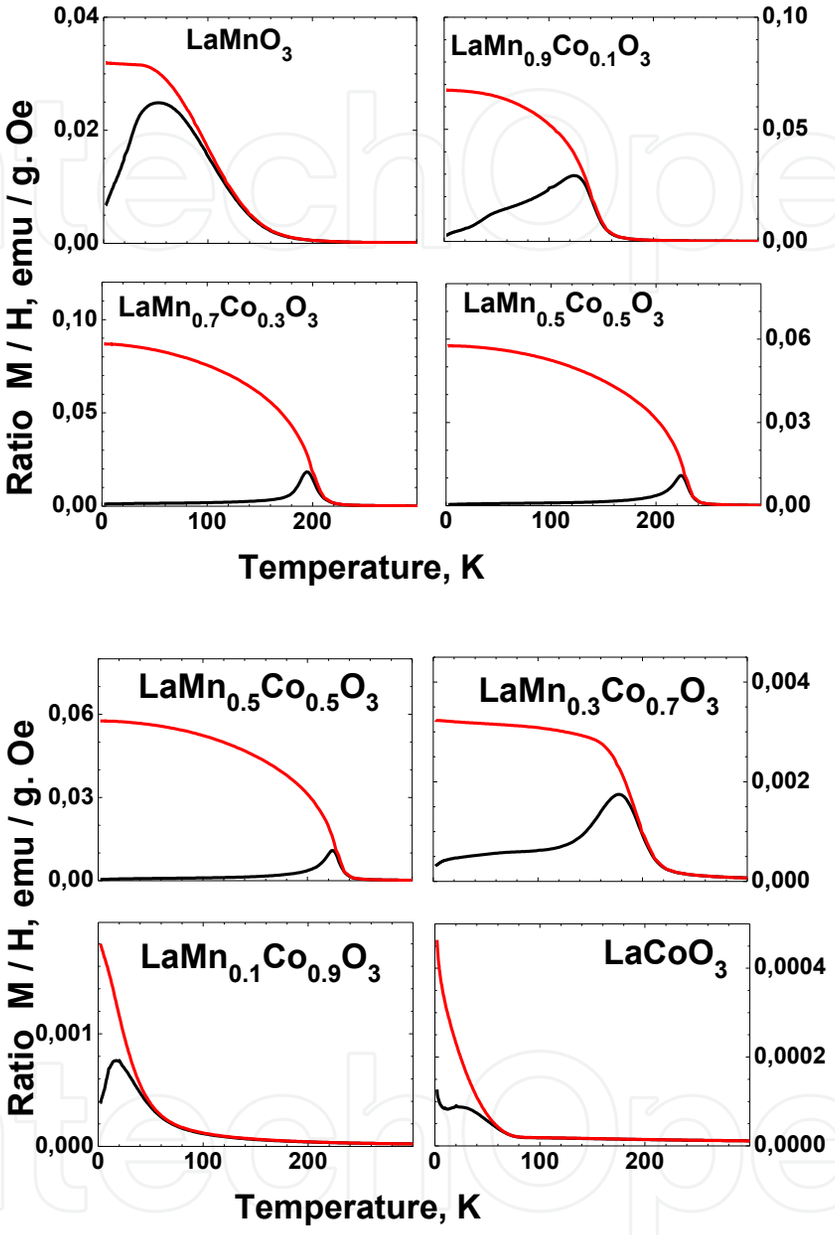

Figure 6. Magnetization cycles for $LaMn_{1-y}Co_yO_3$ measured under 0.025 T: above: y = 0.0, 0.1, 0.3, 0.5; below: y = 0.5, 0.7, 0.9, 1.0

4.5. A- and B-site substitution

Partial substitution of La^{3+} by Ag^+ in $LaMn_{0.9}Co_{0.1}O_3$ substantially increased the catalytic activity in the removal of n-hexane in a flow reactor under an excess of oxygen, attributed to the interaction between O- and the low coordinated metal site. Silver segregated phases further increased the catalytic activity [24].

The BET surface areas of the perovskites varied only slightly with substitution degree. The XRD profiles revealed that the substitution of small amounts of La^{3+} by Ag^{+} cations in a Co-substituted manganite ($LaMn_{0.9}Co_{0.1}O_3$) did not alter its rhombohedral crystallographic structure, and that it only decreased their crystallinity. Segregated silver oxide (Ag_2O) phase was also detected upon increasing the Ag content. TPR profiles indicated that upon introduction of Ag, two features were seen: the first reduction peak shifted toward lower temperatures and became wider upon increasing Ag content; the second reduction peak also started at a lower temperature but became more intense upon increasing Ag content. Since the first reduction step involves the formation of oxygen-deficient perovskite, and the shoulder includes the reduction of individual segregated oxides, quantification of this peak can be taken as a measurement of the extent of Ag insertion in the perovskite structure. The increase in H_2 consumption in the first reduction step upon Ag-substitution is indicative of the appearance of a higher proportion of micro crystals from segregated silver, MnO_2 phases, and/or surface carbonates species. The shift of the peak toward lower temperatures indicates a growth in crystal size. These results are in line with the XRD patterns, which showed diminished crystallinity as silver increased. The FTIR spectra showed an increase in the asymmetric and symmetric O-C-O stretching vibration modes of carboxylate structures with the substitution degree associated with the presence of segregated phases in the form of carbonates in the Ag-substituted perovskites. The XPS spectra of La $3d_{5/2}$ with BE at 834.8 eV and Co $2p_{3/2}$ with BE at 780.6 eV demonstrated the presence of La^{3+} and Co^{3+} species on the surface, whereas manganese appeared at slightly higher BE than is expected for Mn^{3+} ions, suggestive that the surface manganese was present as Mn^{4+}. Differences in the surface O-species upon silver substitution was observed. For the x = 0.0 sample, the two surface oxygen species were the ones expected for a nonsubstituted perovskite. On the other hand, upon Ag substitution, the lower oxidation state of Ag^{+} inserted into the network of the $LaMn_{0.9}Co_{0.1}O_3$ perovskite induced the appearance of O^{2-} species at BE higher than 532 eV known as oxygen vacancies, which is necessary to maintain the electroneutrality of the solid. A relative proportion of this kind of oxygen species of 18% was exhibited by the perovskite with an Ag substitution of x = 0.1, which suggests that the maximum content of Ag with almost no segregated phases was at x = 0.1, and that this segregated phase disappeared at larger quantity of Ag. The EDAX and surface Mn/La and Co/La atomic ratios were much higher than the nominal compositions, and the differences were even larger upon increasing Ag substitution. These results indicate that the surface of the silver-substituted perovskites became Mn- and Ag-enriched, in line with deductions from oxygen-TPD profiles, which showed that Ag-substituted perovskites displayed a new desorption peak associated with the redox cycle of the B cation. This result further indicated that in these perovskites the Mn^{4+}/Mn^{3+} redox cycle was almost constant, in agreement with XPS results. Therefore, the charge compensation due to the substitution of La^{3+} by Ag^{+} occurred mainly via a nonstoichiometric decrease rather than through a change in the Mn^{4+}/Mn^{3+}ratio. The catalytic activity of the perovskites was evaluated in the total combustion of n-hexane in a flow reactor under an excess of oxygen and shown in Fig. 7. The typical S-shaped curves represent the total conversion of n-hexane oxidation as a function of the reaction temperature up to complete combustion. There was an appreciable increase in the catalytic activity, expressed in terms of the total conversion, when Ag was substituted into the

http://dx.doi.org/10.5772/61522

perovskite. For Ag substitution of x = 0.1, a noticeable shift of the curve toward lower temperatures is indicative of a higher catalytic activity of the perovskite upon a 10% Ag substitution of La. The changes in the activity of the $La_{1-x}Ag_xMn_{0.9}Co_{0.1}O_3$ systems are mainly dependent on their crystalline structure and surface composition. The highest activity displayed by the x = 0.3 sample can be explained in terms of the large amount of segregated silver on the surface. Sample x = 0.2 was only slightly less active, although the silver surface segregation was much lower than in its x = 0.3 counterpart. This could be due to the less intense diffraction lines of the rhombohedral phase displayed by the x = 0.3 perovskite. For the sample x = 0.1, in which the rhombohedral structure and almost no silver segregation existed, the relation between catalytic activity and the nonstoichiometric oxygen ratio suggests an intrafacial reaction mechanism.

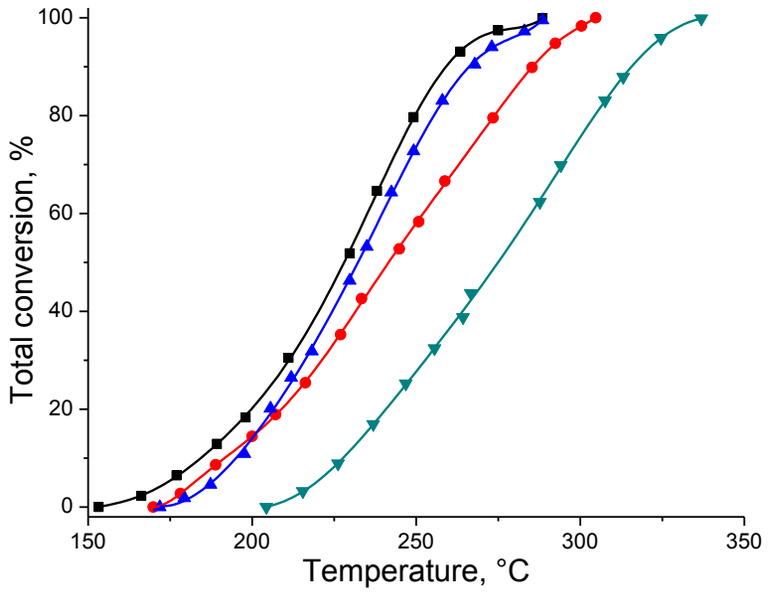

Figure 7. Stationary-state conversion over $La_{1-x}Ag_xMn_{x0.90}Co_{0.1}O_3$ perovskite for (▼) x = 0.0, (●) x = 0.1, (▲) x = 0.2, and (■) x = 0.3.

5. Soot combustion

Diesel engines play a vital role in modern society because they are widely used for heavy-duty transportation and power generation. However, they are one of the largest contributors to environmental pollution because they emit particulate matter and nitrogen oxide. Particulate matter consists mostly of carbonaceous soot, minor amounts of volatile organic fraction from unburned fuel, as well as inorganic compounds such as ash and sulfur compounds. These materials are detrimental to human health, plants physiology, the environment, and building materials [25, 26]. Thus, stringent emission standards for soot have been set by most countries, leading to continuous efforts in emission control technology. Diesel particulate filter (DPF) is the most effective and widely employed approach to reduce soot in exhaust gases. However,

one drawback for using the filter is that it requires regeneration through continuous combustion to remove accumulated soot. Recently, perovskite-type oxides have received considerable attention as catalytic systems for soot combustion [27-29]. Pure and doped lanthanum chromites, manganites, and cobaltites have been tested with mixed results in the catalytic combustion of soot [30]. Cerium has been usually reported as a good promoter in perovskite lattice. Partial substitution of La by Ce or Sr on cobalt-based perovskite led to an increase in catalytic oxidation [31]. When perovskite-type oxides were reduced, their low thermal behavior under reducing atmosphere allowed the formation of highly dispersed metal nanoparticles [22], which consequently modified the oxygen storage capacity of the catalyst. The substitution of the lanthanum cation La^{3+} by an oxygen storage cation such as cerium, with the capacity of the redox Ce^{3+}/Ce^{4+} pair, will have a direct effect in the reducibility of the perovskite structure and the dispersion degree of the pure or mixed La_2O_3 and CeO_2 oxides.

5.1. A-site substitution

The catalytic activity of soot combustion over oxidized and partially reduced substituted $La_{1-x}Ce_xCoO_3$ perovskites is enhanced by two factors: (1) the increase in CeO_2 content, closely related to the increase in the material's capacity for oxygen transfer to the carbonaceous surface; and (2) the formation of larger CeO_2 crystals in the higher-Ce-content samples after H_2 reduction, responsible for the improvement of the exchange of oxygen and number of contact points between catalyst and soot [32].

The BET specific surface areas of the calcined solids ranged from 10 to 19 m^2g^{-1}, and increased upon incorporation of Ce. After reduction, S_{BET} decreased and ranged from 7 to 16 m^2g^{-1}. XRD patterns of the calcined perovskites indicated that Ce was introduced into the lattice of the parent $LaCoO_3$ solid at lower degree of substitution (i.e., $x \leq 0.5$), while for larger Ce content ($x \geq 0.7$) formation of CeO_2 phase was detected. Figure 8 showed the XRD of the (a) calcined and the (b) reduced solids. Larger structural changes after H_2 treatment at 700 ºC were observed for the samples with lower Ce content ($x \leq 0.3$), while calcined and reduced samples with higher Ce content ($x = 0.7$ and 0.9) showed nearly identical XRD patterns. For the samples with lower Ce content ($x = 0.1$, 0.3, 0.5), the most intense diffraction peak of the perovskite-type structure ($2\theta = 33°$) fully disappeared after reduction treatment, and the reduced solids showed the presence of La_2O_3, La_2CoO_4, CeO_2 as segregated phases as well as Co°, which appeared as two broad peaks at $2\theta = 44.3°$ and 51.5°. TPR analysis showed that the reduction of pure $LaCoO_3$ solid occurred in two steps: at 365°C forming an intermediate oxygen-deficient perovskite structure ($LaCoO_{3-\delta}$); and, at 530°C which corresponds to the complete reduction of the perovskite, leading to the formation of La_2O_3, $La(OH)_3$, H_2O, and Co^o. With the addition of Ce, there was a noticeable shift of the peaks to lower temperatures, which implies an increase in the reducibility of the catalysts. The evolution of oxygen during TPD analysis showed a beneficial effect on the presence of α-oxygen with increasing Ce content. The importance of these surface oxygen species is their close relation with the oxygen vacancies in the perovskite structure that can activate molecular oxygen in soot. The catalytic activity determined by nonisothermal thermogravimetric analysis indicated that the activity of calcined catalysts increased with Ce content. $La_{0.1}Ce_{0.9}CoO_3$, the most active catalyst, was the sample with the

http://dx.doi.org/10.5772/61522

highest Ce/La mass ratio and possessed CeO_2 and Co_3O_4 crystalline phases instead of perovskite-type structure (from their XRD patterns). These results suggest that CeO_2 played the main role in soot combustion. The higher activity of the higher Ce-substituted catalysts indicated the availability of reactive oxygen species on the surface of the catalyst, attributed to the weaker binding of oxygen. The enhanced activity of the two catalysts with larger Ce content (x = 0.7 and 0.9) pointed out the importance of structural defects and oxygen mobility by lattice oxygen via La^{3+}-doped CeO_2 in the CeO_2/soot interface for the catalytic oxidation of soot. In order to evaluate the effect of perovskite-type structure on soot combustion, the destruction of the perovskite structure was carried out in hydrogen at 700°C. After reduction, an increase in the catalytic activity was observed in varying degrees: only a slight increase of the activity for the samples with low CeO_2 content (x≤0.5), while the activity for the catalysts with higher amount of CeO_2 (x = 0.7, 0.9) increased sharply. These results suggest that the activity of these materials for soot combustion is improved by increasing the CeO_2 content, closely related to the higher material capacity for oxygen transfer from catalyst to carbonaceous surface and the formation of larger CeO_2 crystals in the higher-Ce-content samples after reduction.

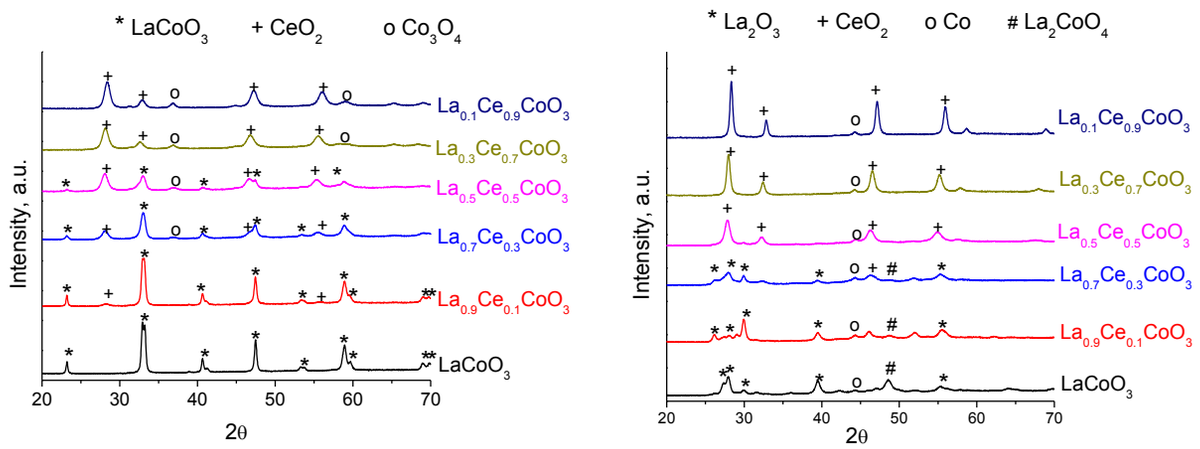

Figure 8. XRD profiles for $La_{1-x}Ce_xCoO_3$ catalysts: (left) calcined; (right) reduced

5.2. A- and B-site substitution

The increase in the catalytic performance in soot combustion by Ag^+ substitution in $LaMn_{0.9}Co_{0.1}O_3$ perovskite structure occurred due to increase in surface Ag species and superoxide ions content. These species have been found to be responsible for the higher capacity for oxygen transfer from the catalyst to the carbonaceous material in the solids with higher-Ag-content [33].

No significant differences between BET specific areas upon Ag substitution were found. XRD profiles revealed that the crystallinity of the rhombohedral structure of the Co-substituted manganite ($LaMn_{0.9}Co_{0.1}O_3$) decreased upon Ag substitution. For the higher Ag-substituted perovskites, the intensities of three diffraction lines- indexed to a segregated Ag_2O phase- increased with increasing Ag substitution: a mean crystal size of 7 nm was estimated by the Debye Scherrer equation at 2θ = 37.96°. The main differences observed in relation to the TPR

profiles of Ag-substituted perovskites with respect to Ag-free perovskite were as follows: the first reduction peak became more intense with increasing x, and the two reduction peaks become closer and shift toward lower temperatures. The increase in H_2 consumption upon Ag-substitution is indicative of the appearance of a higher proportion of Ag_2O segregated crystallites and/or other segregated species. The shift of the peaks toward lower temperatures coincided with the increase in crystallite size; furthermore, it indicates that the redox properties of the solids increased with Ag content. These results were consistent with XRD patterns, which showed a drop in crystallinity of the structure of the perovskites upon increasing silver content, indicating that the Ag^+ inserted into the network made the formation of the perovskite structure more difficult. The BEs from XPS spectra revealed the presence of carbonates strongly attached to the surface, as expected for La-containing perovskites. The core-level spectra indicated the presence of La^{3+} and Co^{3+} species, whereas Mn appeared at slightly higher BE than that expected for Mn^{3+} ions, suggesting that surface Mn was present as Mn^{4+}. Other notable observations were: (i) the $Ag3d_{5/2}$ peaks with BE at 368.2 and 369.3 eV indicated the presence of surface Ag^0 and Ag^+ species, respectively; (ii) the O1s peak was attributed to surface lattice oxygen species (O_{latt}^{2-}) at 529.8 eV, hydroxyl and/or carbonate groups at 531.0–531.4 eV, and loosely adsorbed superperoxide species (O_{2ads}^-) at 532.4–532.6 eV. The surface Ag/La+Ag atomic ratio of the silver-substituted perovskites indicated the enrichment of Ag upon increasing substitution; in addition, the nearly unchanged surface O_{2ads}^-/O_{latt}^{2-} atomic ratio of the Ag-free and the Ag-containing perovskites means that the charge compensation due to the substitution of La^{3+} by Ag^+ occurred via nonstoichiometric decrease rather than through a change in the Mn^{4+}/Mn^{3+} ratio. Since identical trends were obtained for the Ag^+/Ag and the O_{2ads}^-/O_{latt}^{2-} surface ratios for the Ag-containing perovskites, it was proposed that these superoxides ions acted as the most important active species, facilitating oxygen transportation for soot oxidation. In addition, due to the fact that surface Ag and superoxides' ions formation increased with increasing Ag content, surface Ag_2O was proposed as an active phase in the reaction. The evolution O_2-TPD experiments revealed a continuous increase in total α-oxygen species upon Ag doping, supporting the hypothesis of the formation of Ag^+ sites in the lattice of the perovskite. The catalytic activity for soot combustion was related to the temperature corresponding to the maximum from the DTG curve shown in Fig. 9. Higher values for T_m mean lower catalytic activity. T_m value for the uncatalyzed CB combustion was found to be 650°C, while much lower T_m values were observed for all the catalyzed reactions, indicative of the catalytic nature of the materials for soot combustion. Catalytic activity was observed to increase with the silver content, with the best catalyst being the one with Ag content of x = 0.3 (burned off soot at 370°C). This important catalytic effect was attributed to the presence of oxygen vacancies due to the substitution of La^{3+} by Ag^+ in the perovskite lattice. These vacancies enhanced the availability and reactivity of oxygen species on the catalytic surface, because of the weaker oxygen binding. The results show that structural defects and oxygen mobility are important factors that control the catalytic activity of these types of crystalline structures. The presence of surface Ag_2O phase improved the O_2 exchange and number of contact points between catalyst and soot, with no significant effect on BET surface area and crystal size. These results contrast the proposed mechanism for soot combustion on La-containing perovskites,

http://dx.doi.org/10.5772/61522

in which the oxidation of soot particles is attributed to the surface oxygen species, formed on the perovskite structure.

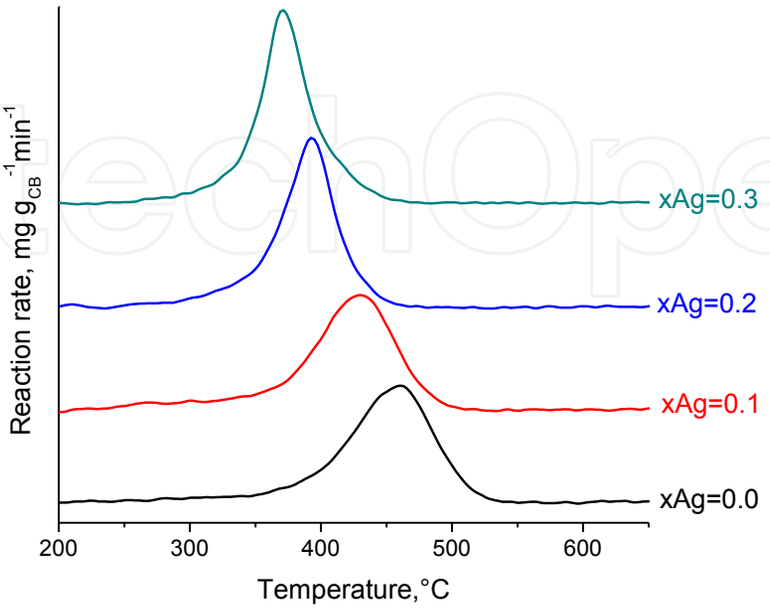

Figure 9. Thermogravimetric assays for the catalytic combustion of CB

6. Hydrogenation reactions

For these kinds of heterogeneous catalytic reactions, perovskite-type oxides are not used directly as catalysts but rather as precursors to obtain metal nanoparticles catalysts. Therefore, prior to the reaction, perovskites are activated *ex situ* under H_2 at 500°C.

7. Guaiacol conversion

Catalytic studies focusing on hydrodeoxygenation (HDO) of guaiacol, the most representative phenolic compound in bio-oil, has provided insights into catalyst optimization for lignin valorization technologies. Different active phases, including sulfides [34-36] and metals [37-39], have been investigated as catalysts for the HDO of guaiacol. Nickel-based catalysts have recently received extensive attention for the HDO of lignin derived compounds, and have consistently been proven to be highly active.

8. A-site substitution

The preparations of Ni catalysts from the reduction of $La_{1-x}Ce_xNiO_3$ perovskite-type oxides were effective in catalyzing the conversion of guaiacol to cyclohexanol, an important feedstock

for the chemical industry. The most active catalyst was the solid with Ce content x = 0.5 and 0.7, which was ascribed to the highest thermal stability under reductive atmosphere of the CeO_2-solid solution partially substituted with La [40].

The BET specific surface areas of the calcined and reduced solids showed a monotonic dependence of the surface area on Ce content with a slight decrease after reduction treatment. The main difference in the XRD patterns of the as-calcined and as-reduced solids after Ce substitution was the absence of the perovskite structure and the appearance of segregated phases in the latter. The most crystalline perovskites corresponded to the undoped $LaNiO_3$ material and the lowest Ce-substituted perovskite ($La_{0.9}Ce_{0.1}NiO_3$). Upon increasing the Ce content ($x \geq 0.5$), there were neither diffraction peaks characteristic of the perovskite structure nor single or mixed La oxides; however, new crystalline phases corresponding to CeO_2 and NiO appeared. The XRD patterns of the Ni-reduced solids indicated a complete loss of the $LaNiO_3$ perovskite structure and the formation of Ni^0 for the material with Ce content x = 0.0 and 0.1. For higher Ce contents (i.e., $x \geq 0.5$), there were no observable changes in the crystalline structure after H_2 treatment, and a shift of the main CeO_2 peak toward higher 2θ angles upon Ce doping can be taken as a clear indication of the modification of the crystalline structures, suggestive of the insertion of La^{3+} into the CeO_2 structure. These results indicate the formation of the perovskite structure with low thermal stability under H_2 for the samples with low Ce content $x \leq 0.3$, and the formation of a solid solution of CeO_2-La_2O_3 with higher thermal stability for samples with higher degree of Ce substitution $x \geq 0.5$. The Ni-reduced catalyst with Ce content x = 0.5 displayed the lowest crystallinity and the highest Ni^0 dispersion. The TPR_1-TPR_2 cycles demonstrated clear differences in the H_2 consumption peaks between TPR cycles, an indication of the structural changes under H_2 treatment. The TPR_1 profiles showed two different behaviors attributed to the reduction of Ni^{2+} to Ni^0: two reduction peaks for the samples with Ce contents $x \leq 0.3$ and only one reduction peak for those with Ce contents $x \geq 0.5$. The amount of H_2 consumed during TPR_1 and TPR_2 cycles is plotted as a function of Ce content and shown in Fig. 10. The TPR_1 profile showed larger H_2 consumption for the perovskites with Ce content $x \leq 0.3$ and almost constant value for those with Ce content $x \geq 0.5$. Considering that the theoretical hydrogen uptake for sample reduction assuming that NiO is stoichiometrically reduced to Ni° is 4.1 mmol g^{-1}, the larger obtained values suggest that other oxides entities are also being reduced. Since XRD results did not show any structural changes under reduction atmosphere, it is possible to calculate the degree of reduction of the perovskite structure considering only the reduction of Ni^{3+} to Ni^0. The obtained reduction degree of 24% fits quite well with previously reported results corresponding to the total reduction of Ni present in the original perovskites. The TEM micrographs of all of the Ni-reduced catalysts showed a narrower particle size distribution for metallic Ni between 5 and 25 nm. The H_2 chemisorption capacity assuming a stoichiometry of $H/Ni_s = 1$ was smaller than the expected one considering the particle size obtained from TEM and XRD, indicating that Ni particles were partially inserted and not available for H_2 uptake. In the conversion of guaiacol over Ni-reduced catalysts, cyclohexanol and methoxycyclohexanol were principally obtained via the hydrogenation and demethylation routes. In other words, the Ni-reduced catalysts displayed a high hydrogenation activity and a low activity toward hydrogenolysis of C-OH bond. The products' distribution calculated both at 20% conversion of guaiacol and at 4 h of reaction time showed

http://dx.doi.org/10.5772/61522

that all the Ni-reduced catalysts displayed similar trends in product distribution. The changes in Ni particle size and the presence of segregated phase influenced by the degree of Ce substitution did not affect the selectivity. This result suggests that the simultaneous presence of highly dispersed nickel partially inserted into a CeO_2-solid solution is a prerequisite for improved catalytic performance for the conversion of guaiacol over these catalytic systems.

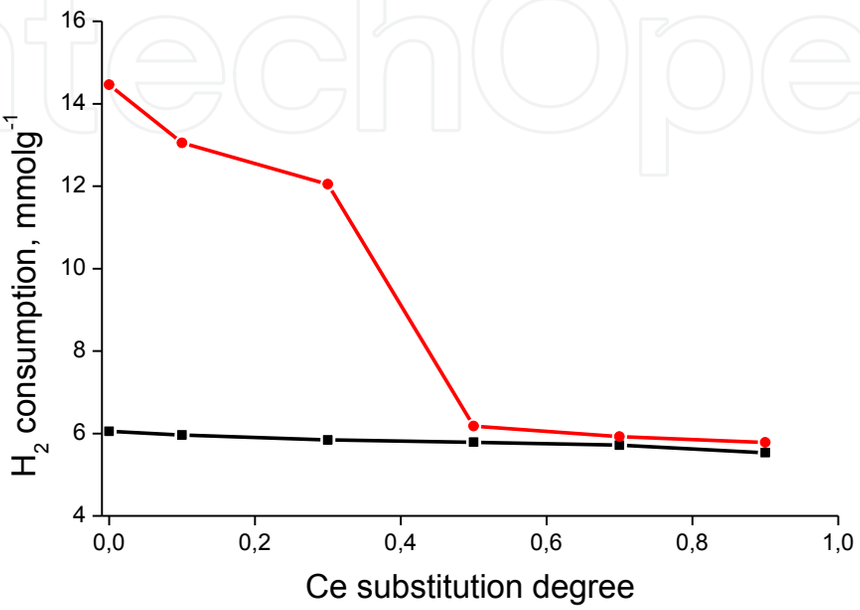

Figure 10. Plot of hydrogen consumption of the $La_{1-x}Ce_xNiO_3$ vs. nominal Ce content (●) TPR_1; (■) TPR_2

9. Glycerol reforming

The use of environmentally friendly and renewable feedstock for clean energy production such as hydrogen has been extensively studied, with particular focus on the catalytic green reforming process of glycerol [41]. Even though the reaction pathway is a complex process, as a result of the occurrence of wide variety of reactions, the type of catalysts used play a key role in determining the product distribution. For supported metal catalysts as well as Ni-based catalysts, high basic character of the catalysts has consistently been observed to lead to higher activity and resistance toward deactivation [42, 43].

9.1. A-site substitution

Mixed oxides with the general formula $La_{1-x}Ce_xNiO_3$ used as precursors for supported Ni catalysts have led to active catalysts for the production of hydrogen-rich gas stream. Substitution of 50% of La by Ce provided more deactivation-resistant catalyst, allowing only minor amount of deactivation, associated with the formation of CeO_2-La_2O_3 solid solutions, which acted as an oxygen buffer and, hence, facilitated the removal of carbon deposits on the catalysts surface [44].

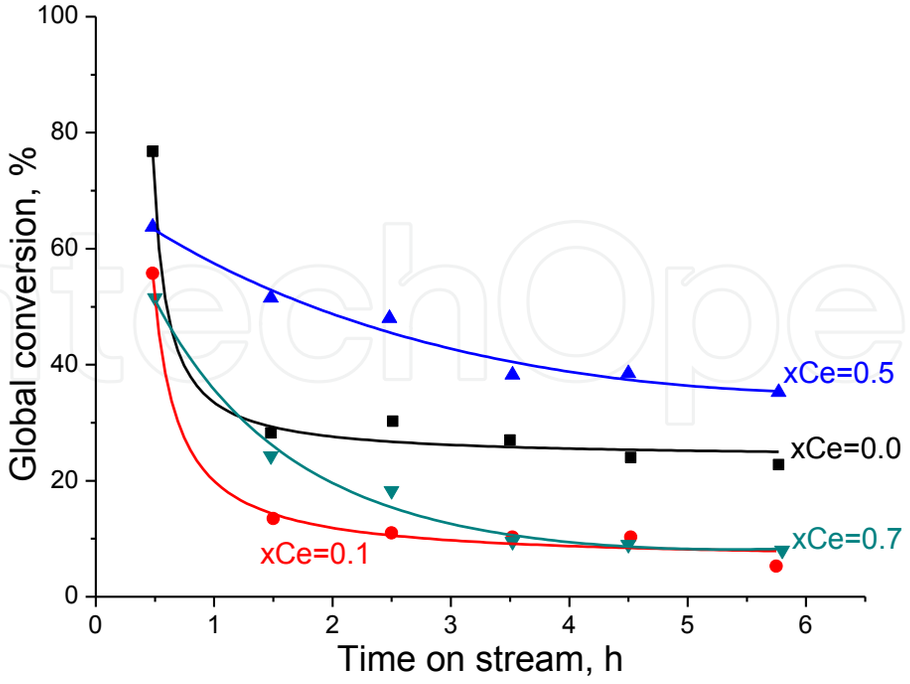

Figure 11. Evolution of global glycerol conversion as a function of time on stream for glycerol steam reforming at 500 °C over all mixed oxide-derived catalysts

The $La_{1-x}Ce_xNiO_3$ perovskites used as precursors for supported Ni catalysts were previously fully characterized and used as catalysts in glycerol steam reforming. Figure 11 illustrates the global performance of the catalysts for glycerol reforming. Regardless of the features of the catalysts or degree of La substitution by Ce, a drop in global conversion versus time on stream was observed. However, the sample formed from the mixed oxide with an equivalent content of La^{3+} and Ce^{3+} (x=0.5) was much more stable and promising, which may be associated with the formation of a CeO_2-La_2O_3 solid solution as detected by XRD analysis. The catalysts with Ce substitution other than 50% led to a dramatic decrease in glycerol conversion, revealing a strong deactivation process: indeed x = 0.1 and x = 0.7 samples presented conversion within 5 and 20% right after the first hour. To investigate the causes of deactivation, Fe-SEM analysis revealed that the deactivation of unsubstituted $LaNiO_3$ perovskite-derived catalysts (x = 0.0) was due to the formation of plentiful amounts of filamentous carbon. Even though, the formation of the carbon nanostructures did not occur equally over all Ce-containing catalysts due to varying degrees of Ce substitution, considerable amounts of carbon filaments and similar FE-SEM images were obtained even for unsubstituted $LaNiO_3$ perovskite-derived catalyst (x=0.0). Conversely, after a much more detailed and meticulous analysis, only few filaments could be found on the x = 0.5 solid. Thus, it can be argued that although deactivation occurred irrespective of catalysts composition, the sample with 50% La substituted by Ce was more resistance to deactivation compared to other loadings. TEM micrographs allowed the identification of carbon nanotubular structures with an open end, where it was suggested that Ni nanoparticles were detached. From this analysis, it was suggested that Ni nanoparticles were intimately involved in the formation of those carbon filaments. TPO/TGA analyses combined with mass spectrometry were complementarily performed for the used catalysts.

http://dx.doi.org/10.5772/61522

The evolution of CO_2 (m/z=44) observed in the analysis originated from the gasification of carbon deposits. The x = 0.5 sample possessed the lowest amount of the more reactive carbon deposits. Thus, the minimization of the deactivation process in glycerol reforming requires an appropriate Ce content, which can lead to the formation of CeO_2-La_2O_3 solid solutions.

10. Xylose hydrogenation

Liquid phase hydrogenation of aldoses is an important process in the synthesis of mono- and disaccharides, which have long been used as natural sweetening agents. Xylitol, an excellent sweet molecule, can also be commercialized because its sweetening capacity exceeds that of sugar by 20-25%, in addition to having no insulin requirements [45]. Several well-known hydrogenation catalysts such as noble metals or nickel-based [46] catalysts have been used for xylose hydrogenation [47]. Due to their lower price, the main advantage of Ni catalysts is their utilization in a typical slurry batch reactor, leading to good activity and selectivity. Nevertheless, the major drawback of Ni catalysts (which has been reported for Raney Ni) is their high deactivation rate as a result of poisoning of the active sites and metal leaching.

10.1. A-site substitution

A series of active and selective partially Ni-substituted $La_{1-x}Ce_xAl_{0.18}Ni_{0.82}O_3$ perovskite catalysts with a constant Ni loading of 20 wt.% were tested in the hydrogenation of xylose to xylitol to gain insight into the importance of the perovskite structure in preventing leaching.

The specific surface areas obtained showed that the solids with lower Ce substitution degree displayed lower values between 9 and 15 m^2g^{-1}, while higher values above 30 m^2g^{-1} were obtained for solids with higher Ce substitution degrees. The XRD patterns of the reduced solids shown in Figure 12 indicated that the Ce-free solid presented perovskite structure while upon Ce substitution segregated phases appeared. The x = 0.1 solid showed both the perovskite phase and the presence of mixed oxides. For larger Ce substitution degree the perovskite structure was not present and only peaks corresponding to Ce-La oxide solid solution were found. TPR results show only two reduction peaks corresponding to reduction of Ni species. TEM micrographs revealed that Ni was dispersed on the oxide support without forming nanoparticles. Catalytic activity results indicated that all the catalysts were active in the hydrogenation of xylose to xylitol. The catalysts with lower Ce substitution degree (x=0.0, 0.1) displayed higher catalytic activity, demonstrating the importance of crystalline perovskite structure in this reaction. Xylitol selectivity between 40 and 60% was obtained at a conversion of 30%. Hydrogenolysis products were also detected. Atomic absorption spectroscopy (AAS) analysis of the catalyst before and after reaction indicated that for the unsubstituted and lower Ce substituted solids (x = 0.0, 0.1), a constant Ni content close to the nominal loading was obtained, indicative of the high stability under aqueous medium. On the other hand, the solid with the higher Ce substitution degree (x = 0.5, 0.7) showed loss of Ni by leaching. The results from this study demonstrated clear dependence on the reactivity and stability of the catalyst on the presence of crystalline perovskite, modulated by the degree of Ce substitution.

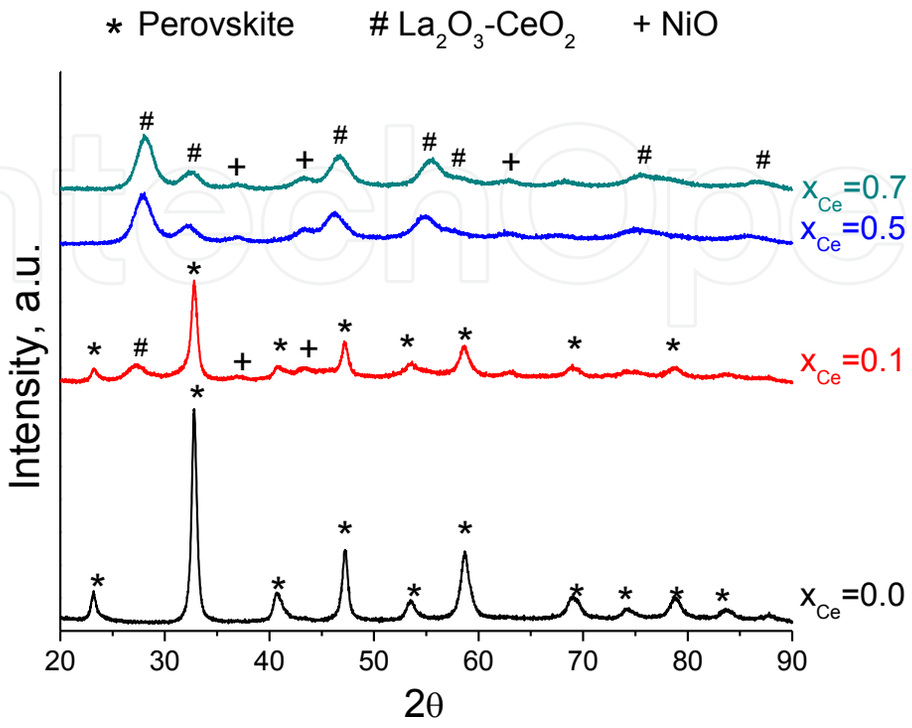

Figure 12. XRD pattern of Ni-substituted $La_{1-x}Ce_xAl_{0.18}Ni_{0.82}O_3$ catalyst

11. Conclusion

Perovskite-type oxides with La in the A-site and a d-transition metal in the B-site position are the most widely used materials for catalytic purposes. The activity of La perovskites can be noticeably improved by partial replacement of the A-site and/or B-site metal. The different combinations of partial substitution of A-site by an adequate A' metal with similar ionic radii but lower oxidation state modifies the oxidation state of the B-site metal cation and/or oxygen vacancies formation. This substitution also affects the thermal stability, crystalline structure, and activity of the perovskites. Two clear applications can be identified:

- Perovskites with oxygen vacancies to be used as catalysts in oxidation reactions
- Perovskites to be used as precursors to prepare nanosized catalysts to be used in hydrogenation reactions

Due to their tunable properties, perovskites show different crystallization structures and high flexibility in their composition, and, hence, it is important to understand how different perovskites behave under different reaction conditions and what would be the most effective metal combination for a given catalytic process.

Acknowledgements

The authors thank CONICYT Fondecyt No 1130005 and Red Doctoral REDOC, and the MINEDUC project UCO1202.

Author details

Gina Pecchi[1*], Nestor Escalona[2,3], I. Tyrone Ghampson[2] and Ruddy Morales[1]

*Address all correspondence to: gpecchi@udec.cl

1 Dpto Físico Química, Facultad Ciencias Químicas, Universidad de Concepción, Concepción, Chile

2 Dpto Ingeniería Química y Bioprocesos, Escuela de Ingeniería, Pontificia Universidad Católica de Chile, Macul, Santiago, Chile

3 Facultad de Química, Pontificia Universidad Católica de Chile, Santiago, Chile

References

[1] Voorhoeve RJH, Remeika JP, Trimble LE, Cooper AS, Disalvo FJ, Gallagher PK. Perovskite-like La1−xKxMnO3 and related compounds: Solid state chemistry and the catalysis of the reduction of NO by CO and H2. *J Solid State Chem*. 1975 8//;14(4): 395-406.

[2] John R. Anderson MB. M. *Dry*: Springer-Verlag Berlin Heidelberg; 1981.

[3] Escalona N, Medina C, García R, Reyes P. Fischer Tropsch reaction from a mixture similar to biosyngas. Influence of promoters on surface and catalytic properties of Co/SiO2 catalysts. *Catalysis Today*. 2009 5/15/;143(1–2):76-9.

[4] Medina C, García R, Reyes P, Fierro JLG, Escalona N. Fischer Tropsch synthesis from a simulated biosyngas feed over Co(x)/SiO2 catalysts: Effect of Co-loading. *Appl Catalys A: General*. 2010 1/31/;373(1–2):71-5.

[5] Ubilla P, Garcia R, Fierro JLG, Escalona N. Hydrocarbons synthesis from a simulated biosyngas feed over FE/SIO2, catalysts. *J Chilean Chem Soc*. 2010;55:35-8.

[6] Bedel L, Roger AC, Estournes C, Kiennemann A. Co0 from partial reduction of La(Co,Fe)O3 perovskites for Fischer–Tropsch synthesis. *Catalysis Today*. 2003 10/15/;85(2–4):207-18.

[7] Bedel L, Roger AC, Rehspringer JL, Kiennemann A. Structure-controlled La-Co-Fe perovskite precursors for higher C2-C4 olefins selectivity in Fischer-Tropsch synthe-

sis. In: Xinhe B, Yide X, editors. *Studies in Surface Science and Catalysis*. Volume 147: Elsevier; 2004. p. 319-24.

[8] Escalona N, Fuentealba S, Pecchi G. Fischer–Tropsch synthesis over LaFe1−xCoxO3 perovskites from a simulated biosyngas feed. *Appl Catalysis A: General*. 2010 6/15/;381(1–2):253-60.

[9] Yu L, Diao G, Ye F, Sun M, Zhou J, Li Y, et al. Promoting Effect of Ce in Ce/OMS-2 Catalyst for Catalytic Combustion of Dimethyl Ether. *Catal Lett*. 2011 2011/01/01;141(1):111-9. English.

[10] Liang JJ, Weng H-S. Catalytic properties of lanthanum strontium transition metal oxides (La1-xSrxBO3; B = manganese, iron, cobalt, nickel) for toluene oxidation. *Indus Engin Chem Res*. 1993 1993/11/01;32(11):2563-72.

[11] Teraoka Y, Nii H, Kagawa S, Jansson K, Nygren M. Influence of the simultaneous substitution of Cu and Ru in the perovskite-type (La,Sr)MO3 (M Al, Mn, Fe, Co) on the catalytic activity for CO oxidation and CO–NO reactions. *Appl Catalys A: General*. 2000 3/13/;194–195:35-41.

[12] Wu Y, Yu T, Dou B-s, Wang C-x, Xie X-f, Yu Z-l, et al. A comparative study on perovskite-type mixed oxide catalysts A′xA1 − xBO3 − λ (A′ = Ca, Sr, A = La, B = Mn, Fe, Co) for NH3 oxidation. *J Catalys*. 1989 11//;120(1):88-107.

[13] Tejuca LG, Fierro JLG, Tascón JMD. Structure and Reactivity of Perovskite-Type Oxides. In: D.D. Eley HP, Paul BW, editors. *Advances in Catalysis*. Volume 36: Academic Press; 1989. p. 237-328.

[14] Kharton VV, Viskup AP, Naumovich EN, Tikhonovich VN. Oxygen permeability of LaFe1−xNixO3−δ solid solutions. *Mater Res Bull*. 1999 10/8/;34(8):1311-7.

[15] Rao CNR, Gopalakrishnan J. *New Directions in Solid State Chemistry*. Cambridge University Press; 1997.

[16] Yu Z, Gao L, Yuan S, Wu Y. Solid defect structure and catalytic activity of perovskite-type catalysts La1-SrNiO3-[small lambda] and La1-1.333ThNiO3-[small lambda]. *J Chem Soc Faraday Trans*. 1992;88(21):3245-9.

[17] Popa M, Frantti J, Kakihana M. Lanthanum ferrite LaFeO3+d nanopowders obtained by the polymerizable complex method. *Solid State Ionics*. 2002 12/2/;154–155:437-45.

[18] Sumathi R, Johnson K, Viswanathan B, Varadarajan TK. Selective oxidation and dehydrogenation of benzyl alcohol on ABB′O3 (A=Ba, B=Pb, Ce, Ti and B′=Bi, Cu, Sb)-type perovskite oxides-temperature programmed reduction studies. *Appl Catalysis A: General*. 1998 8/24/;172(1):15-22.

[19] Pecchi G, Reyes P, Zamora R, Campos C, Cadús LE, Barbero BP. Effect of the preparation method on the catalytic activity of La1−xCaxFeO3 perovskite-type oxides. *Catalysis Today*. 2008 4//;133–135:420-7.

[20] Pecchi G, Jiliberto MG, Delgado EJ, Cadús LE, Fierro JLG. Effect of B-site cation on the catalytic activity of La1−xCaxBO3 (B = Fe, Ni) perovskite-type oxides for toluene combustion. *J Chem Technol Biotechnol*. 2011;86(8):1067-73.

[21] Pecchi G, Reyes P, Zamora R, Cadús LE, Fierro JLG. Surface properties and performance for VOCs combustion of LaFe1−yNiyO3 perovskite oxides. *J Solid State Chem*. 2008 4//;181(4):905-12.

[22] Pecchi G, Campos C, Peña O. Thermal stability against reduction of LaMn1−yCoyO3 perovskites. *Mater Res Bull*. 2009 4/2/;44(4):846-53.

[23] Pecchi G, Campos C, Peña O, Cadus LE. Structural, magnetic and catalytic properties of perovskite-type mixed oxides LaMn1−yCoyO3 (y = 0.0, 0.1, 0.3, 0.5, 0.7, 0.9, 1.0). *J Mol Catalys A: Chemical*. 2008 3/3/;282(1–2):158-66.

[24] Pecchi G, Campos CM, Jiliberto MG, Delgado EJ, Fierro JLG. Effect of additive Ag on the physicochemical and catalytic properties of LaMn0.9Co0.1O3.5 perovskite. *Appl Catalys A: General*. 2009 12/15/;371(1–2):78-84.

[25] Li Q, Meng M, Dai F, Zha Y, Xie Y, Hu T, et al. Multifunctional hydrotalcite-derived K/MnMgAlO catalysts used for soot combustion, NOx storage and simultaneous soot–NOx removal. *Chem Engin J*. 2012 3/1/;184:106-12.

[26] Li Z, Meng M, Dai F, Hu T, Xie Y, Zhang J. Performance of K and Ni substituted La1−xKxCo1−yNiyO3−δ perovskite catalysts used for soot combustion, NOx storage and simultaneous NOx-soot removal. *Fuel*. 2012 3//;93:606-10.

[27] Pecchi G, Cabrera B, Buljan A, Delgado EJ, Gordon AL, Jimenez R. Catalytic oxidation of soot over alkaline niobates. *J Alloys Compounds*. 2013 2/25/;551:255-61.

[28] Pecchi G, Cabrera B, Delgado EJ, García X, Jimenez R. Activity of KNbO3 as catalyst for soot combustion: Effect of the preparation method. *Appl Catalys A: General*. 2013 2/26/;453:341-8.

[29] Taniguchi K, Okinaka N, Akiyama T. Preparation and characterization of La1−xKxFeO3 (x = 0–1) by self-propagating high-temperature synthesis for use as soot combustion catalyst. *J Alloys Compounds*. 2011 3/10/;509(10):4084-8.

[30] Fino D, Russo N, Saracco G, Specchia V. The role of suprafacial oxygen in some perovskites for the catalytic combustion of soot. *J Catalys*. 2003 7/25/;217(2):367-75.

[31] Zhang R, Luo N, Chen B, Kaliaguine S. Soot Combustion over Lanthanum Cobaltites and related oxides for diesel exhaust treatment. *Energy Fuels*. 2010 2010/07/15;24(7): 3719-26.

[32] Pecchi G, Morales R, Delgado EJ, Jimenez R, Fraga M. Catalytic combustion of soot onCe-doped Lanthanum Cobaltites. *J Chilean Chem Soc*. 2014;59:2725-30.

[33] Pecchi G, Dinamarca R, Campos CM, Garcia X, Jimenez R, Fierro JLG. Soot oxidation on silver-substituted LaMn0.9Co0.1O3 perovskites. *Indus Engin Chem Res*. 2014 2014/06/18;53(24):10090-6.

[34] Bui VN, Laurenti D, Afanasiev P, Geantet C. Hydrodeoxygenation of guaiacol with CoMo catalysts. Part I: Promoting effect of cobalt on HDO selectivity and activity. *Appl Catalys B: Environmental*. 2011 1/14/;101(3–4):239-45.

[35] Laurent E, Delmon B. Study of the hydrodeoxygenation of carbonyl, carylic and guaiacyl groups over sulfided CoMo/γ-Al2O3 and NiMo/γ-Al2O3 catalysts: I. Catalytic reaction schemes. *Appl Catalys A: General*. 1994 2/17/;109(1):77-96.

[36] Sepúlveda C, Escalona N, García R, Laurenti D, Vrinat M. Hydrodeoxygenation and hydrodesulfurization co-processing over ReS2 supported catalysts. *Catalysis Today*. 2012 11/15/;195(1):101-5.

[37] Gutierrez A, Kaila RK, Honkela ML, Slioor R, Krause AOI. Hydrodeoxygenation of guaiacol on noble metal catalysts. *Catalysis Today*. 2009 10/15/;147(3–4):239-46.

[38] Lee CR, Yoon JS, Suh Y-W, Choi J-W, Ha J-M, Suh DJ, et al. Catalytic roles of metals and supports on hydrodeoxygenation of lignin monomer guaiacol. *Catalys Commun*. 2012 1/5/;17:54-8.

[39] Nimmanwudipong T, Runnebaum RC, Block DE, Gates BC. Catalytic conversion of guaiacol catalyzed by platinum supported on alumina: Reaction network including hydrodeoxygenation reactions. *Energy Fuels*. 2011 2011/08/18;25(8):3417-27.

[40] Escalona N, Aranzaez W, Leiva K, Martínez N, Pecchi G. Ni nanoparticles prepared from Ce substituted LaNiO3 for the guaiacol conversion. *Appl Catalys A: General*. 2014 7/5/;481:1-10.

[41] Simonetti DA, Kunkes EL, Dumesic JA. Gas-phase conversion of glycerol to synthesis gas over carbon-supported platinum and platinum–rhenium catalysts. *J Catalys*. 2007 4/25/;247(2):298-306.

[42] Dieuzeide ML, Jobbagy M, Amadeo N. Glycerol steam reforming over Ni/γ-Al2O3 catalysts, modified with Mg(II). Effect of Mg (II) content. *Catalys Today*. 2013 9/15/;213:50-7.

[43] Iriondo A, Güemez MB, Barrio VL, Cambra JF, Arias PL, Sánchez-Sánchez MC, et al. Glycerol conversion into H2 by steam reforming over Ni and PtNi catalysts supported on MgO modified γ-Al2O3. In: E.M. Gaigneaux MDSHPAJJAM, Ruiz P, editors. *Studies in Surface Science and Catalysis*. Volume 175: Elsevier; 2010. p. 449-52.

[44] Franchini CA, Aranzaez W, Duarte de Farias AM, Pecchi G, Fraga MA. Ce-substituted LaNiO3 mixed oxides as catalyst precursors for glycerol steam reforming. *Appl Catalys B: Environmental*. 2014 4/5/;147:193-202.

[45] Mikkola J-P, Sjöholm R, Salmi T, Mäki-Arvela P. Xylose hydrogenation: kinetic and NMR studies of the reaction mechanisms. *Catalysis Today*. 1999 1/27/;48(1–4):73-81.

[46] Wisniak J, Hershkowitz M, Leibowitz R, Stein S. Hydrogenation of xylose to xylitol. *Product R&D.* 1974 1974/03/01;13(1):75-9.

[47] Wisniak J, Hershkowitz M, Stein S. Hydrogenation of xylose over platinum group catalysts. Product R&D. 1974 1974/12/01;13(4):232-6.

IntechOpen

IntechOpen